ACS Photonics

pubs.acs.org/journal/apchd5

Perspective

Wavefront Engineering for Scintillation-Based Imaging

Joshua Chen,* Sachin Vaidya, Simo Pajovic, Seou Choi, William Michaels, Louis Martin-Monier, Juejun Hu, Carol Cogswell, Charles Roques-Carmes, and Marin Soljačić

Cite This: *ACS Photonics* 2026, 13, 1757−1766

Read Online

ACCESS | Metrics & More | Article Recommendations | Supporting Information

ABSTRACT: Recent research in nanophotonics for scintillation-based imaging has demonstrated promising improvements in scintillator performance. In parallel, advances in nanophotonics have enabled wavefront control through metasurfaces, a capability that has transformed fields such as microscopy by allowing tailored control of optical propagation. This naturally raises the following question, which we address in this Perspective: can wavefront-control strategies be leveraged to improve scintillation-based imaging? To answer this question, we explore nanophotonic- and metasurface-enabled wavefront control in scintillators to mitigate image blurring arising from their intrinsically diffuse light emission. While depth-of-field extension in scintillation faces fundamental limitations absent in microscopy, this approach reveals promising avenues, including stacked scintillators, selective spatial-frequency enhancement, and X-ray energy-dependent imaging. These results clarify the key distinctions in adapting wavefront engineering to scintillation and its potential to enable tailored detection strategies.

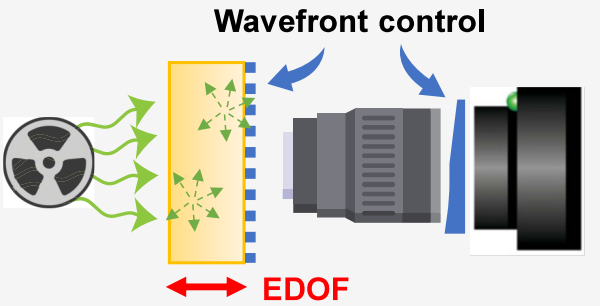

KEYWORDS: *Scintillation, Wavefront Control, X-ray Imaging, Nanophotonics, Metaoptics, Inverse Design*

INTRODUCTION

Scintillation is the process by which certain materials, called scintillators, absorb ionizing radiation such as X-ray or γ-ray photons and re-emit the deposited energy as visible light detectable by standard photodiodes or camera sensors. This enables indirect measurement of radiation that is otherwise difficult to detect.[1] Scintillators are therefore widely used as radiation detectors and are central components in many medical imaging systems including X-ray radiography, computed tomography (CT), and positron emission tomography (PET). In these imaging applications, scintillator performance metrics such as light yield and absorption efficiency directly impact clinical image quality, radiation dose, and ultimately the effectiveness of disease diagnosis and treatment.

Recent work has shown that nanophotonic structuring can substantially change how scintillators emit light and, in turn, improve the detector performance. By patterning the scintillator or an adjacent layer on the scale of the scintillation wavelength, one can reshape the photonic environment in two main ways: (i) nanostructures can modify the local density of optical states seen by the scintillation transitions, speeding up and spectrally reshaping spontaneous emission;[2,3] and (ii) they can introduce additional outcoupling channels that redirect light toward the detector[4] or allow for better optical coupling. This "nanophotonic scintillator" approach has been explored using plasmonic structures,[5−7] photonic crystals,[2,4,8−11] and inverse-designed nanophotonic stacks.[12,13] Together, these studies have demonstrated up to order-of-magnitude increases in light yield,[3−7,9,11,12] improved control over angular emission,[4,8,11] and scalable routes to patterning.[9−11] Recent analyses estimate that current CT usage may account for roughly 100,000 radiation-induced cancers per year in the U.S., corresponding to up to ∼5% of all new cancers,[14,15] underscoring the urgency of improving detector performance. To date, however, this work has largely focused on controlling the emission rate, spectrum, and light extraction, leaving scintillation wavefront engineering largely unexplored.

Wavefront engineering refers to shaping how emitted light propagates through the imaging system and is encoded at the detector. More broadly, wavefront engineering encompasses the deliberate modification of the optical wavefront—typically through pupil-plane phase or amplitude control—to tailor the system point spread function (PSF) for a given imaging task. Rather than maximizing image sharpness alone, wavefront engineering redistributes desired optical information in a controlled manner so that it can be more effectively recovered through computation. In scintillation-based imaging, wavefront engineering can extend beyond the scintillator itself to the full imaging pipeline, encompassing the X-ray source, scintillator

Received: December 28, 2025
Revised: March 2, 2026
Accepted: March 3, 2026
Published: March 16, 2026

https://doi.org/10.1021/acsphotonics.5c03124
ACS Photonics 2026, 13, 1757−1766

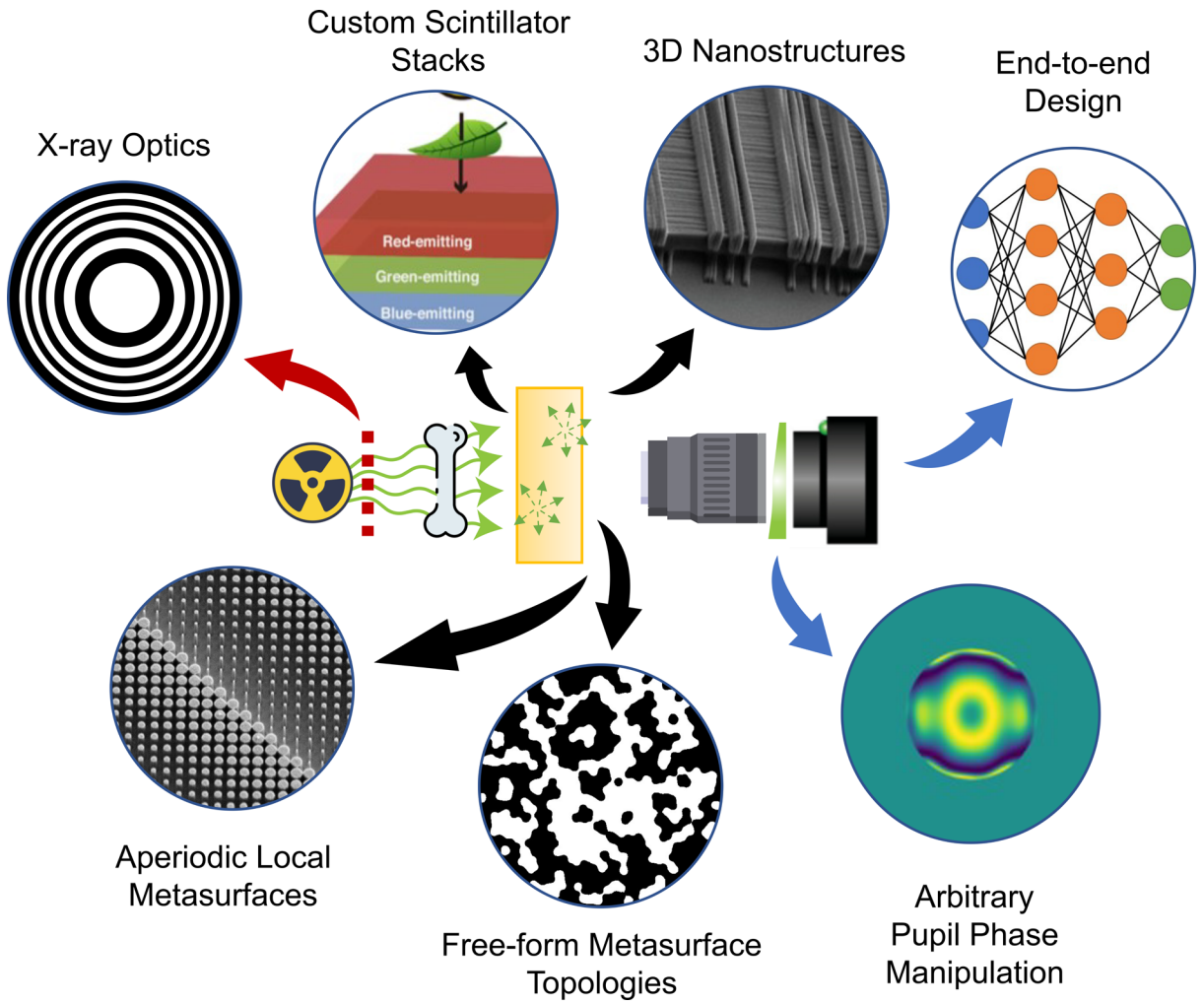

Figure 1. Wavefront engineering in scintillation-based X-ray imaging. Schematic highlighting wavefront control in scintillation: tailoring X-ray sources with dedicated optics (here we show a zone plate common for X-ray focusing), designing custom scintillators (e.g., multicolor stacks), and integrating end-to-end computational design. On the detection side, aperiodic, free-form, and 3D nanostructures together with arbitrary pupil-phase control provide further degrees of freedom for shaping scintillation light. The inset for "Custom Scintillator Stacks" is adapted from ref 13, reproduced under a Creative Commons Attribution 4.0 International License (CC BY 4.0). The inset for "3D Nanostructures" is adapted with permission from ref 16. Copyright © 2022 American Chemical Society.

architecture, detection optics, and reconstruction algorithms. Figure 1 provides a schematic overview of this broad design space.

A key enabler of practical wavefront engineering is the emergence of fabrication techniques for metasurfaces and related nanophotonic optical elements that allow compact, lithographically defined control of the optical phase at subwavelength resolution. Aperiodic local metasurfaces,[17,18] free-form or inverse-designed phase profiles,[19,20] and three-dimensional nanophotonic structures[16,21,22] have all been demonstrated at length scales corresponding to the characteristic emission wavelength of scintillators, with many fabrication approaches compatible with wafer-scale processing and large-area patterning. These advances make it feasible to implement sophisticated wavefront-control strategies directly at the detection stage of scintillation systems or in close integration with structured scintillators.

It is important to acknowledge that direct detectors, such as silicon and cadmium zinc telluride (CZT), are relevant alternatives to scintillators. These materials convert radiation directly to electrical charge, avoiding the isotropic light spread that fundamentally limits the spatial resolution of bulk scintillators—an advantage that has driven the recent introduction of photon-counting computed tomography (PCCT). However, the relative advantages of direct-conversion and scintillator-based systems are often application-dependent, and each technology carries distinct physical, engineering, and economic trade-offs. Direct-conversion detectors can offer major advantages in spatial resolution and, in photon-counting implementations, intrinsic spectral information. At the same time, there remain important trade-offs that can favor scintillator-based approaches in many imaging regimes. First, common semiconductors like silicon have significantly lower stopping power than high-Z scintillators, which reduces dose efficiency at medical X-ray energies.[23] Second, while high-Z direct materials like CZT offer excellent stopping power and spectral sensitivity, they are difficult to grow as large, defect-free single crystals, leading to substantially higher manufacturing costs compared to standard scintillator fabrication.[24] Third, under the extreme X-ray fluxes typically encountered for rapid clinical imaging, direct detectors operating in the photon-counting mode are

https://doi.org/10.1021/acsphotonics.5c03124
ACS Photonics 2026, 13, 1757−1766

susceptible to charge sharing and pulse pile-up. In contrast, scintillators operating in current-integration mode naturally handle large photon fluxes without saturation or pile-up errors.[25] In this context, nanophotonics offers a promising strategy to improve scintillator-based detectors: by applying wavefront control to scintillators, one preserves the inherent robustness, stopping power, and practical cost advantages that continue to make scintillators highly attractive in many imaging settings while addressing the optical resolution limits that have historically challenged their performance.

In optical microscopy, wavefront engineering has been widely used to extend imaging capabilities beyond those achievable with conventional diffraction-limited optics. By shaping the pupil-plane phase, the system PSF can be engineered to encode additional information into the image, which is later recovered computationally. Prominent examples include engineered PSFs for three-dimensional single-molecule localization, which encode the axial position into the image of a point emitter,[26,27] as well as adaptive optics, where programmable wavefront corrections compensate for aberrations to preserve high resolution deep within biological tissue.[28] These approaches illustrate how redistributing optical information—rather than simply sharpening the PSF—can enable new imaging functionalities.

This observation naturally prompts the question of whether analogous wavefront-engineering strategies could address long-standing limitations in scintillation-based X-ray imaging. Scintillation systems face optical-blurring challenges that are reminiscent of depth-of-field constraints in microscopy. To efficiently stop X-rays, scintillators must be millimeters thick, but the visible photons they emit are generated isotropically and can propagate laterally over significant distances before reaching the detector. As scintillator thickness increases, this lateral spread leads to image blur and degraded spatial resolution, creating a fundamental trade-off between X-ray stopping power and imaging resolution.[12]

In this Perspective, we investigate the use of wavefront engineering for scintillation-based imaging and find that there are fundamental limitations that stem from the depth-distributed nature of scintillation emission. Using wavefront coding as a representative example, we identify when wavefront engineering can provide new functionalities and when fundamental differences between scintillation and conventional microscopy make them ineffective. Guided by these insights, we outline new avenues for wavefront engineering in scintillation including stacked multicolor scintillators, selective enhancement of specific spatial frequencies, and X-ray-energy-dependent imaging.

WAVEFRONT CODING: A REPRESENTATIVE EXAMPLE

Wavefront coding is a technique that extends the depth of field of an imaging system by deliberately making the PSF invariant over a wide range of depths.[29] Because the PSF hardly changes as the object moves in or out of focus, the recorded image can later be processed with a matching computational operation (e.g., deconvolution) to reconstruct a sharp image over that entire depth range. A seemingly natural extension of wavefront coding to scintillation-based imaging would be to design an imaging system with an extended depth of field that spans the entire scintillator thickness. In principle, such a system would bring emission from all depths into focus simultaneously, allowing their contributions to be combined without blurring from isotropic scintillation light and potentially recovering high-resolution images even in thick scintillators.

Figure 2 outlines similarities between scintillation-based imaging and microscopy, where a scintillator is coupled to

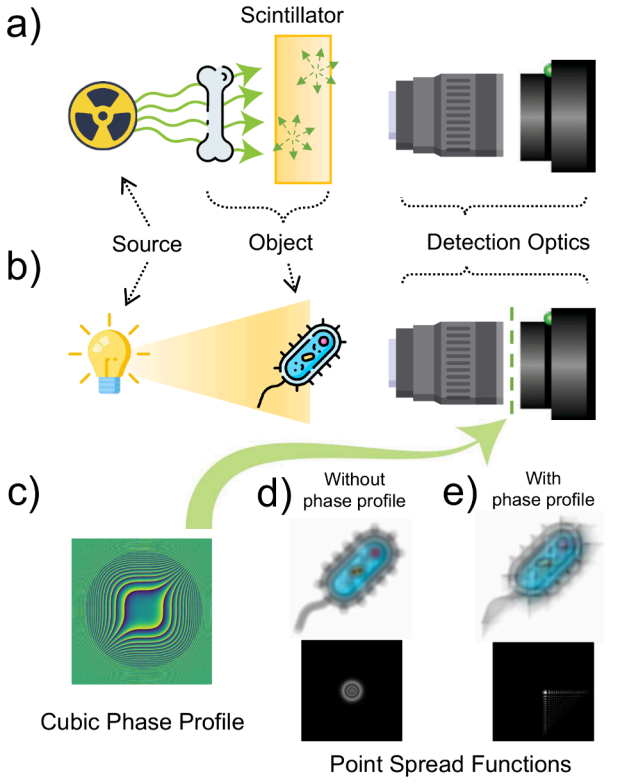

Figure 2. Similarities between scintillation-based imaging and microscopy. (a) In scintillators imaged by, for example, free-space optics, light emission from the scintillator is collected and focused to the detector. (b) In microscopy, detection optics similarly image a biological specimen, and wavefront engineering can be used to enhance certain functionalities. (c) A cubic phase profile can be inserted to modify the system point spread function to be depth-invariant. (d) Without a phase profile, the PSF results in standard image defocus, but (e) with a cubic phase profile, the PSF is altered to be invariant to defocus, allowing an extended depth of field (EDOF) to be achieved through computational reconstruction. The ground truth image can be found in (b).

imaging free-space optics. In scintillation-based imaging, the object is encoded in the "shadow" of X-rays incident on the scintillator and emitted according to the depth-dependent characteristics of the scintillator. This is analogous to the imaging of a three-dimensional fluorescent object in emissive microscopy such as fluorescence microscopy. Furthermore, wavefront coding can be applied to alter the PSF of the system in microscopy, allowing for computational methods to extract the desired information. We show the acquired image measurements as well as the associated PSFs with and without a cubic phase mask designed to enable extended depth of field in Figure 2d and e.

Since scintillation is an incoherent emission process, the response of the imaging system is linear in intensity. We model the scintillator as a discrete stack of incoherently emitting planes spanning its thickness, as shown first in Figure 3b. Each plane forms an image at the detector according to its associated point spread function, denoted $h_z(\mathbf{r})$ for emission originating at depth z, which encodes the depth-dependent optical blur

https://doi.org/10.1021/acsphotonics.5c03124
ACS Photonics 2026, 13, 1757−1766

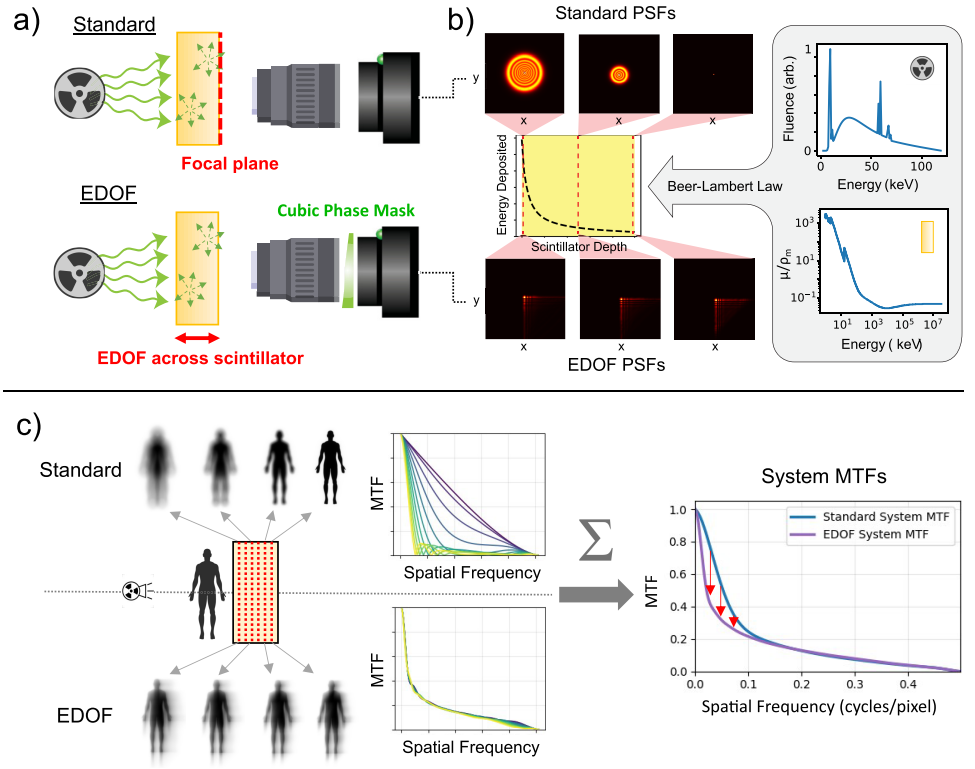

Figure 3. Extended depth of field (EDOF) for scintillation-based imaging. (a) Comparison between scintillation using standard detection optics versus scintillation with extended depth of field (EDOF) capabilities. (b) Point spread functions along discrete scintillator planes for standard detection (top) and EDOF detection (bottom). The depth-dependent energy deposition in the scintillator is modeled using the source X-ray spectrum and the energy-dependent scintillator mass attenuation coefficients. (c) Comparison between discrete planar standard and EDOF modulation transfer functions (MTF). Different color lines in the MTF plots correspond to the various discrete planes in the scintillator. Despite the apparent advantage of the discrete planar MTFs in the EDOF case, the system MTF of the standard system lies above the system MTF of the EDOF system at all spatial frequencies.

and can be modeled within the framework of Fourier optics.[30] The intensity of each plane is set by the fluence of X-rays absorbed at that depth, which can be estimated from the source X-ray spectrum, scintillator X-ray mass attenuation coefficients, and Beer−Lambert law. This model is validated by a multiphysics Geant4[31] and Zemax OpticStudio[32] ray-tracing pipeline that considers all relevant scintillation physics, described in Supplement S1.

While Figure 2a depicts a free-space optical readout—common in micro-CT and high resolution laboratory imaging systems—we note that the depth-resolved model introduced above is not specific to this configuration. Many scintillation detectors instead employ direct coupling between the scintillator and the image sensor, where lateral blur arises from near-field scintillator light spreading, internal scattering, and sensor integration rather than from defocus through an imaging lens. In both cases, however, the recorded image is formed as an incoherent sum over the emission depth, with each depth contributing a characteristic impulse response $h_z(\mathbf{r})$. The framework developed here therefore applies broadly across detector architectures. Wavefront engineering, whether implemented through free-space meta-optics or via nano-photonic structures patterned directly on or within the scintillator, acts by reshaping these depth-dependent responses and the resulting system PSF.

Figure 3a demonstrates the application of wavefront coding with a cubic phase mask to scintillation and compares it with standard detection optics. In the standard case (top), the imaging system has a single focal plane, whereas wavefront coding extends the depth of field across the scintillator (bottom). Figure 3b shows the PSFs of select discrete planes along the depth of the scintillator. In the standard case (top row), the PSFs vary strongly in size with depth, while in the wavefront-coded case (bottom row), they exhibit the characteristic cubic PSF shape and remain nearly invariant across the entire thickness. When the emission from all planes is summed, this depth-invariant PSF would, in principle, allow deconvolution to recover the full image.

LIMITS OF IMAGE RECONSTRUCTION IN SCINTILLATION-BASED IMAGING

A key distinction between scintillation and conventional imaging modalities like microscopy is the integration of depth information at the detector, which fundamentally alters how wavefront coding can be applied in scintillation-based imaging. This difference arises once we consider the full imaging workflow, which includes a reconstruction step (typically deconvolution) to generate a final image. Figure 3c illustrates how wavefront coding can shape the modulation transfer function (MTF), which quantifies how an imaging system transfers object contrast to the image as a function of spatial frequency. In the standard imaging system (top plot), the image blur varies with emission depth in the scintillator: the in-focus plane has a high MTF, while the out-of-focus planes show a rapid loss of contrast. In the extended depth of field (EDOF) system (bottom plot), the object image remains

https://doi.org/10.1021/acsphotonics.5c03124
ACS Photonics 2026, 13, 1757−1766

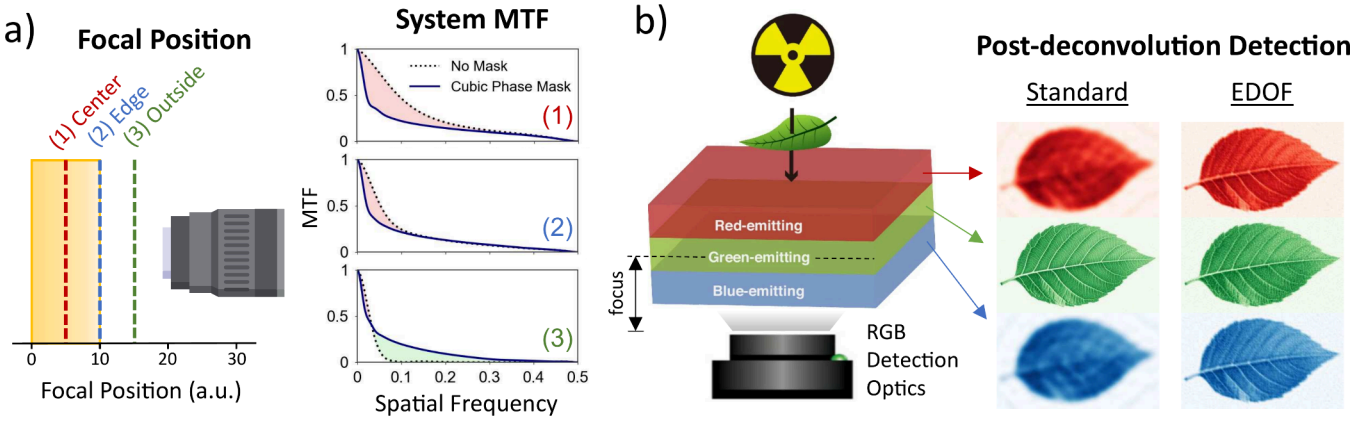

Figure 4. Use cases for EDOF in scintillation-based imaging. (a) When the desired focal plane lies outside the scintillator volume, the extended depth of field becomes beneficial, as seen in the system MTFs comparing the standard and cubic phase mask designs. (b) The same principle extends to stacked multicolor scintillator systems where, without EDOF, the scintillator layers away from the chosen focal plane are severely out of focus.

nearly unchanged for all emission planes, because the PSFs are depth-invariant. The corresponding MTFs are likewise consistent across planes and, importantly, exhibit no zeros in spatial frequency, a typical requirement for stable image reconstruction.

However, the picture is different once we include the reconstruction process in the comparison. The key distinction lies in how PSF is used in reconstruction. In microscopy, computational postprocessing is performed with a single in-focus PSF, which can be directly measured. For example, in Wiener deconvolution,[33] the PSF is used in its Fourier-space representation as H_0:

$$\hat{O}(\mathbf{k}) = \frac{H_0^*(\mathbf{k})}{|H_0(\mathbf{k})|^2 + \gamma} I(\mathbf{k}) \tag{1}$$

where $\hat{O}(\mathbf{k})$ is the reconstructed image in the spatial-frequency domain, $\mathbf{k}$ denotes the spatial frequency coordinate, γ is a regularization parameter related to the noise-to-signal power ratio, and $I(\mathbf{k})$ is the measured image in the Fourier domain. The form of this Wiener deconvolution, along with the underlying assumptions, is summarized in Supplement S2.

In scintillation, however, the measured image is an incoherent sum of contributions from all depths, so linearity of convolution leads to a single effective system PSF (Figure 3b) given by a fluence-weighted sum of the depth-dependent PSFs:

$$h_{\text{sys}}(\mathbf{r}) = \sum_z w_z h_z(\mathbf{r}) \tag{2}$$

where $h_z(\mathbf{r})$ is the PSF for emission originating at depth z, and w_z is the corresponding fluence weighting. Since $I(\mathbf{k})$ is approximated by $O(\mathbf{k})\ H_{\text{sys}}(\mathbf{k})$ in scintillation, deconvolution must therefore be performed with the Fourier-space representation $H_{\text{sys}}(\mathbf{k})$, rather than the single-plane PSF $H_0(\mathbf{k})$. Put simply, depth in microscopy carries new information, whereas depth in scintillation carries only redundancy and blur, since all scintillator depths image the same transverse object.

In practice, traditional deconvolution with the system PSF given by eq 2 yields little to no improvement in resolution: the system's MTF is below that of the standard (nonwavefront-coded) system at all spatial frequencies, shown in Figure 3c. While widefield fluorescence microscopy also involves incoherent emission from multiple depths, wavefront coding is typically applied in regimes where depth information is either sparse, recoverable, or explicitly reconstructed. In scintillation-based imaging, depth is irreversibly integrated prior to detection, fundamentally altering the role of wavefront engineering. This fundamental difference constrains how wavefront coding can be used for resolution enhancement in scintillation, but it also points to new potential functionalities for wavefront engineering in scintillator design.

WAVEFRONT ENGINEERING FOR SCINTILLATION-BASED IMAGING

Extended Depth of Field (EDOF) in Scintillation-Based Imaging

In this section, we highlight how one can adapt wavefront coding to applications in scintillation-based imaging, leading to new performance metrics and use cases with distinct functionalities. In all of the following examples, we use Wiener deconvolution[33] for postprocessing, since it depends only on the system PSF and noise statistics. (Other algorithms that incorporate stronger priors may perform better for specific tasks, but we do not consider them here to simplify the comparison.) Throughout, we use the system MTF as the primary performance metric for wavefront-engineered scintillation because it directly quantifies the robustness of each spatial frequency to noise in the system. Since the phase-only pupil modifications considered here do not change the total detected photon flux or the underlying detector noise sources, we assume a design-independent noise power spectrum (NPS), under which the system MTF serves as a straightforward proxy for the fundamental performance metric of detective quantum efficiency (DQE).[34]

The traditional use of wavefront coding for depth-of-field extension is most useful when none of the relevant emitting scintillator planes are sharply imaged by the system. If the focus of the imaging system lies inside the scintillator, then some emission planes are already well focused; thus, wavefront coding only smears information that is already sharp. On the other hand, if the focus lies outside the scintillator, then no emission plane is well focused, and wavefront coding can preserve high-frequency information that would otherwise be lost. Figure 4a illustrates this point. The shaded yellow band on the left marks the scintillator thickness, and the dashed lines

https://doi.org/10.1021/acsphotonics.5c03124
ACS Photonics 2026, 13, 1757−1766

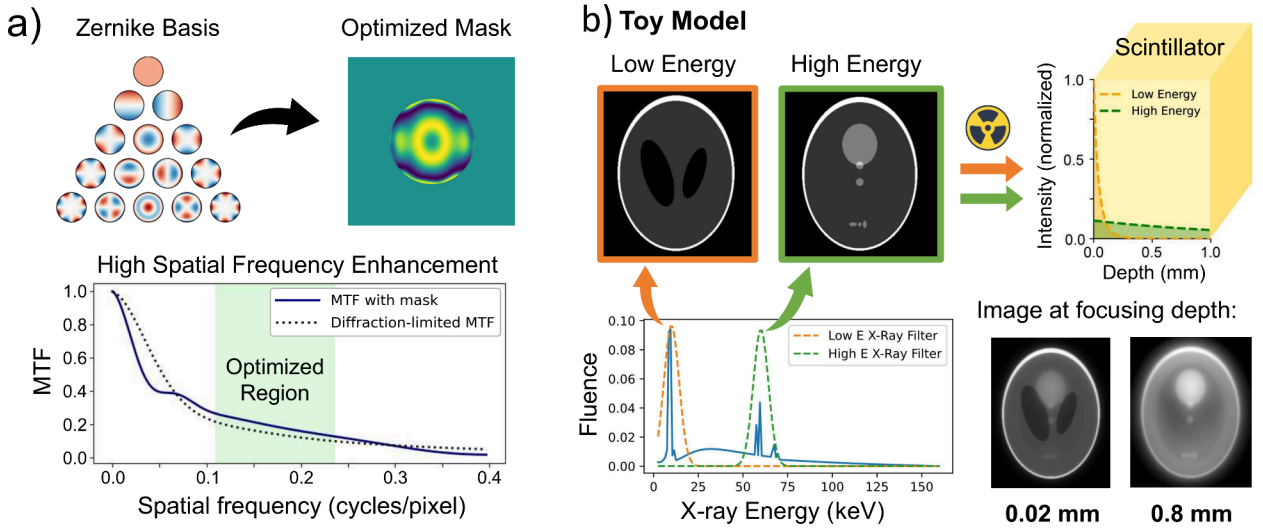

Figure 5. (a) Inverse design using the Zernike basis can optimize for certain spatial frequencies above the in-focus optimal MTF. (b) A toy model demonstrates energy-dependent scintillation imaging, where some features of the Shepp-Logan phantom are carried by high energy X-rays, and some features are carried by low energy X-rays. The X-ray energy deposited for each portion of the Shepp-Logan phantom is plotted on the yellow rectangular prism, representing the scintillator. The detected image thus varies according to the plane of focus in the scintillator.

labeled (1)−(3) indicate three possible focus planes of the objective: in the center of the scintillator, at its edge, and outside it. The three panels on the right show, for each focus position, the system MTF of a standard objective (dotted black) and of the same objective with a cubic phase mask (solid blue). When the focus lies inside the scintillator (cases (1) and (2)), the cubic-mask MTF stays below the standard objective MTF at all spatial frequencies; therefore, wavefront coding only degrades the information that is already in focus. When the focus lies outside the scintillator in case (3), no emission plane is sharply imaged, so the unmasked system strongly suppresses high spatial frequencies in H_{sys}. In this regime, the cubic phase mask redistributes defocus blur more evenly across depth, leading to a larger $|H_{sys}(\mathbf{k})|$ at high spatial frequencies than for the standard objective. Thus, the extended depth of field through wavefront coding is beneficial only when the defocused information does not already appear sharply at some in-focus plane of the system—a guideline that applies to all applications of wavefront coding.

This observation has important implications for stacked scintillator systems. Such stacks have been explored for energy-resolving detection, where scintillators with different emission characteristics are combined to recover information about X-ray attenuation,[35−38] enabling energy resolution and material decomposition.[39] As with single-layer scintillators, stacked designs still face a trade-off between thickness and spatial resolution. This trade-off can be even more severe when light generated in one scintillator must traverse another scintillator layer before reaching the detector.

For example, Min et al.[13] recently proposed a multicolor scintillator stack coupled to a red-green-blue (RGB) detector, consisting of three layers emitting approximately in the red, green, and blue spectral bands. This work offers a concrete example of a stacked scintillator architecture with a spectrally separated readout. Figure 4b shows a proof-of-concept implementation of such a multicolor stack and the corresponding postdeconvolution images for both a standard imaging system and an EDOF system using a cubic phase profile. As seen in the leaf images, the red- and blue-emitting layers suffer from severe loss of spatial resolution without an EDOF design.

Having identified use cases where traditional wavefront coding benefits scintillation and adopted the system MTF as our figure of merit, we now ask what pupil phase profile might be optimal for scintillation.

Inverse Design of Wavefront Encoders for Scintillation-Based Imaging

Having established the system MTF as our figure of merit, we can use inverse design[40] methods to automatically discover a pupil phase profile for enhanced scintillation-based encoding by maximizing a cost function of the system MTF. Rather than restricting ourselves to a specific mask such as a cubic phase profile, we turn to gradient-based inverse design enabled by our autodifferentiable simulation framework introduced in Figure 3b. In general, the choice of the inverse design algorithm depends on the parameter space and the intended reconstruction strategy. For the continuous phase profiles considered here, where the goal is optimizing linear deconvolution or direct image quality metrics, gradient-based local optimization is favorable due to its efficiency and ability to efficiently navigate high-dimensional spaces. We therefore employ this approach using the Method of Moving Asymptotes (MMA).[41] Conversely, end-to-end optimization of optics with nonlinear neural network reconstructors typically utilizes stochastic gradient descent,[42] while designs involving discrete or binary nanostructures often require derivative-free global search algorithms like genetic algorithms or particle swarm optimization as the discrete nature of the parameters prevents the direct calculation of gradients.

For optimization, we parametrize the pupil phase using the standard Zernike basis,[43] a set of orthogonal polynomials widely used to represent optical aberrations. Zernike modes provide an efficient, nonredundant expansion of pupil phase variations and help reduce parameter coupling during optimization. Using the Zernike basis shown in Figure 5a, we optimize the Zernike coefficients up to the 15th order (136 basis functions in total) to maximize the system MTF for

https://doi.org/10.1021/acsphotonics.5c03124
ACS Photonics 2026, 13, 1757−1766

scintillation. We define the optimization objective as the integrated system MTF over spatial frequencies,

$$\mathcal{L}_{\mathrm{MTF}} = \int_0^{k_{\max}} \mathrm{MTF}_{\mathrm{sys}}(k)\, \mathrm{d}k$$

where $\mathrm{MTF}_{\mathrm{sys}}(k)$ is the system MTF and $k_{\max}$ denotes the maximum spatial frequency represented in the discretized Fourier domain. Performing optimization reveals two key insights:

1. Maximizing the Integrated System MTF over All Spatial Frequencies Always Shifts the Plane of Focus to the Average Intensity Depth in the Scintillator. Among all 136 Zernike basis functions, only the basis function responsible for defocus (Z_2^0) significantly affects the integrated MTF, acting effectively as an additional lens term that adjusts the focal length of the system. This means the optimization does not introduce higher-order phase structure but instead selects a "plane of best focus" inside the scintillator. We find empirically that this optimized plane coincides with the average emission depth, given by

$$x_{\mathrm{optimal}} = \frac{\int_0^d x s(x)\, \mathrm{d}x}{\int_0^d s(x)\, \mathrm{d}x} \tag{3}$$

where $s(x)$ is the scintillation energy weighting as a function of depth and d is the scintillator thickness (for example, $s(x) = \frac{1}{m} e^{-x/m}$ for a monochromatic X-ray energy with a mean attenuation length m). A natural interpretation of this result is that focusing near the average emission depth minimizes the cumulative blur in the final image by balancing the contributions from all emitting planes. This "optimal plane" has important implications for wavefront engineering with metasurfaces or other aperiodic nanophotonic structures fabricated directly on scintillators.

2. Certain Spatial Frequencies Can Be Enhanced through Inverse Design. In conventional wavefront coding, no phase mask can increase the system MTF at any spatial frequency beyond the in-focus, diffraction-limited MTF because the two-dimensional optical transfer function (whose magnitude is the MTF) is the autocorrelation of the pupil function within the paraxial framework.[30] Any additional phase in the pupil can only introduce destructive interference and reduce the MTF at various spatial frequencies: as derived in Supplement S3 there exists a bound

$$\mathrm{MTF}(\mathbf{k}) \leq \mathrm{MTF}_{\mathrm{DL}}(\mathbf{k}) \;\forall\; \mathbf{k}$$

where $\mathbf{k}$ denotes the transverse spatial frequency vector in the image plane, $\mathrm{MTF}(\mathbf{k})$ denotes the modulation transfer function for an arbitrary pupil phase, and $\mathrm{MTF}_{\mathrm{DL}}(\mathbf{k})$ is the diffraction-limited MTF corresponding to a uniformly phased pupil, for which the magnitude of the pupil autocorrelation is maximized.

In scintillation systems, however, this constraint can be relaxed because the image formation process is intrinsically depth-dependent. As shown in Figure 5a, when we choose an objective function that emphasizes a specific spatial-frequency band, inverse design yields phase profiles that boost the system MTF above the in-focus MTF of the standard system within that band at the expense of spatial frequencies outside the optimized range. This targeted enhancement suggests that scintillation systems can be tailored to preferentially transmit particular spatial scales—corresponding to specific feature or object sizes such as anatomical structures, lesions, or growths—with higher fidelity than would otherwise be possible.

Building on these insights from inverse design, we next examine how the optimal plane shifts when the depth-weighting $s(x)$ changes with X-ray energy and how this can be exploited for energy-dependent imaging.

X-ray Energy Encoding with Wavefront Engineering

Up to this point, we have treated the scintillator response as if it were independent of distinct X-ray energies. However, identifying distinct X-ray energies can provide substantial additional information, enabling material discrimination and quantitative imaging.[36,37,39] In our framework, X-ray photons of different energies are associated with different scintillator mass attenuation coefficients; therefore, they deposit energy at different depths and thus contribute different depth weightings $s(x)$. Through eq 3, this immediately implies that each X-ray energy (or energy band) has its own optimal plane of focus inside the scintillator, given by its own average emission depth.

To illustrate this, we consider a simplified toy model in which different spatial features of an object are carried by different X-ray energy bands (whereas in reality, low- and high-energy photons will be correlated through the material mass attenuation coefficients). Figure 5b shows a segmented Shepp-Logan phantom[44] in which small features are associated with higher-energy X-rays and large features with lower-energy X-rays. Because the energy-dependent attenuation coefficients differ across the segments, each band produces a distinct depth profile, $s(x)$, and therefore a different optimal focus plane according to eq 3. Guided by this equation, we select two imaging depths in a 1 mm-thick scintillator: one near the front facet at 0.02 mm and one near the back facet at 0.80 mm. It is important to note that this depth selection is optical, rather than a physical rejection of photons. The detector integrates the total flux from the entire scintillator volume, and thus the total signal remains constant regardless of the focal setting. The focal plane selection instead ensures that features at the selected depth appear sharp, while emission from other depths appears as a defocused background. Consequently, the signal-to-background ratio for specific features is maximized at their optimal focal plane, thereby improving the signal-to-noise ratio for the desired features given a constant detector read noise. Therefore, as seen in the simulated images, changing the focus between these depths selectively sharpens different sets of features, corresponding to different energy bands and thus different material information.

This example shows that wavefront engineering in scintillation exposes a new handle for energy-dependent imaging: the choice of focal plane implicitly selects an "average" X-ray energy and the associated material information encoded at that depth. The depth−energy structure of scintillation then becomes a tunable channel, where focusing at different planes emphasizes different energy bands and, in turn, different features or materials in the object.

OUTLOOK

Our results show that wavefront engineering in scintillation must be approached differently than in microscopy. As shown, direct application of wavefront-coding strategies fails because scintillation images are formed as incoherent sums over the emission depth. When viewed at the system level, however,

https://doi.org/10.1021/acsphotonics.5c03124
ACS Photonics 2026, 13, 1757−1766

wavefront engineering still opens a rich and structured design space for scintillator-based imaging. By working with the system PSF and MTF, we identified when extended depth of field is actually beneficial, how depth-dependent blurring in stacked scintillators can be mitigated, how inverse design reveals an "optimal" focus plane set by the depth distribution of scintillation, and how specific spatial frequencies can be selectively emphasized. We also showed that these ideas naturally extend to X-ray energy-dependent imaging, where the optimal wavefront pattern is tied to the average emission depth of a given energy band.

Furthermore, this system-level approach fundamentally alters the traditional scintillator trade-off between X-ray stopping power and imaging resolution previously discussed. In conventional scintillation detection, increasing the scintillator thickness to boost signal conversion inevitably results in geometric blurring due to the isotropic spread of light. By contrast, wavefront engineering decouples these parameters: the scintillator thickness determines the stopping power, while the lateral resolution is fundamentally limited by the numerical aperture of the optical system. While the theoretical upper limit is thus defined by diffraction, the practical performance limit is dictated by additional system-specific constraints such as the X-ray energy spectrum and exact detector configuration. Here, the inverse design allows us to computationally optimize for a specific hardware configuration, ensuring the system approaches its fundamental physical limit.

We highlight a broad landscape of directions for advancing scintillation-based imaging enabled by wavefront engineering. Across the imaging pipeline, new degrees of freedom are becoming accessible that make it possible to shape, encode, and interpret scintillation light in ways that have yet to be explored. On the detector side, recent demonstrations of nanophotonic structuring directly within scintillators—including volumetric and three-dimensional architectures—establish the feasibility of embedding complex functionality at the point of emission.[45] More broadly, continued progress in nanofabrication, including nanoimprint lithography,[46] colloidal and block copolymer self-assembly,[47,48] and two-photon lithography,[49] is expanding the set of wavefront- and emission-shaping structures that can be realized in or on scintillators. A range of material platforms have already been used for optical phase and scattering control in this context, including dielectric platforms such as SiN, TiO_2, and SiO_2 patterned as layers on scintillators, direct structuring of common scintillator materials (e.g., garnets and other oxides), and structured templates that can be infused with liquid scintillators to realize composite architectures. Crucially, these fabrication advances facilitate the monolithic integration of the scintillator and detector layers. Such unified architectures eliminate the scattering and reflection losses associated with discrete interfaces, optical adhesives, or air gaps, maximizing photon transfer efficiency and ensuring that the benefits of wavefront engineering are preserved at the detection stage. In parallel, emerging work on stacked and other architected scintillator systems demonstrates how depth, spectrum, and emission pathways can be codesigned at the material level, providing a complementary axis for encoding information prior to detection.[13] Beyond the scintillator itself, pupil-phase manipulation and end-to-end optical-computational codesign offer additional levers for task-specific encoding and reconstruction.[50−52] Similar principles could also be extended upstream, where engineered X-ray illumination or source-side structuring might be codesigned with scintillator architectures and detection optics to better align scintillation light for specific imaging tasks. Taken together, these directions point toward a shift from treating scintillation as a fixed light source to viewing it as an integral, designable component of the imaging system, with wavefront engineering providing a unifying framework for understanding performance limits and guiding future detector architectures.

■ ASSOCIATED CONTENT

Supporting Information

The Supporting Information is available free of charge at https://pubs.acs.org/doi/10.1021/acsphotonics.5c03124.

Validation of the autodifferentiable scintillation model, mathematical derivation of the Wiener deconvolution reconstruction algorithm used, and a formal proof of the diffraction-limited MTF upper bound for phase masks (PDF)

■ AUTHOR INFORMATION

Corresponding Author

Joshua Chen − *Research Laboratory of Electronics, MIT, Cambridge, Massachusetts 02139, United States;* orcid.org/0000-0001-7547-6503; Email: chenjosh@mit.edu

Authors

Sachin Vaidya − *Research Laboratory of Electronics and Department of Physics, MIT, Cambridge, Massachusetts 02139, United States*

Simo Pajovic − *Department of Mechanical Engineering, MIT, Cambridge, Massachusetts 02139, United States;* orcid.org/0000-0002-7497-3118

Seou Choi − *Research Laboratory of Electronics, MIT, Cambridge, Massachusetts 02139, United States*

William Michaels − *Research Laboratory of Electronics, MIT, Cambridge, Massachusetts 02139, United States*

Louis Martin-Monier − *Department of Materials Science and Engineering, MIT, Cambridge, Massachusetts 02139, United States*

Juejun Hu − *Department of Materials Science and Engineering, MIT, Cambridge, Massachusetts 02139, United States;* orcid.org/0000-0002-7233-3918

Carol Cogswell − *Department of Electrical, Computer and Energy Engineering, University of Colorado Boulder, Boulder, Colorado 80309, United States*

Charles Roques-Carmes − *Research Laboratory of Electronics, MIT, Cambridge, Massachusetts 02139, United States; Ginzton Laboratory, Stanford University, Stanford, California 94305, United States;* orcid.org/0000-0002-1168-5944

Marin Soljačić − *Research Laboratory of Electronics and Department of Physics, MIT, Cambridge, Massachusetts 02139, United States;* orcid.org/0000-0002-7184-5831

Complete contact information is available at: https://pubs.acs.org/10.1021/acsphotonics.5c03124

Funding

This work was supported by the U.S. Army Research Office through the Institute for Soldier Nanotechnologies at MIT under Collaborative Agreement Number W911NF-23-2-0121. J.C. and W.M. acknowledge support from the NSF GRFP

under Grant Number 2141064. S.P. acknowledges the MathWorks Engineering Fellowship. S.C. acknowledges support from the Korea Foundation for Advanced Studies Overseas Ph.D. Scholarship. C.R.-C. is supported by a Stanford Science Fellowship.

Notes

The authors declare no competing financial interest.

■ ACKNOWLEDGMENTS

The authors would like to thank Dr. Tom Vettenburg, Dr. Steven E. Kooi, and Chris Hogan for stimulating discussions. ChatGPT (OpenAI) and Gemini (Google) were used for clarity and language edits; all scientific content and conclusions are those of the authors.

■ REFERENCES

(1) Weber, M. J. Inorganic scintillators: today and tomorrow. *J. Lumin.* **2002**, *100*, 35−45.
(2) Kurman, Y.; Shultzman, A.; Segal, O.; Pick, A.; Kaminer, I. Photonic-crystal scintillators: Molding the flow of light to enhance X-ray and γ-ray detection. *Phys. Rev. Lett.* **2020**, *125*, No. 040801.
(3) Kurman, Y.; Lahav, N.; Schuetz, R.; Shultzman, A.; Roques-Carmes, C.; Lifshits, A.; Zaken, S.; Lenkiewicz, T.; Strassberg, R.; Be'er, O.; Bekenstein, Y.; Kaminer, I. Purcell-enhanced X-ray scintillation. *Sci. Adv.* **2024**, *10*, No. eadq6325.
(4) Roques-Carmes, C.; Rivera, N.; Ghorashi, A.; Kooi, S. E.; Yang, Y.; Lin, Z.; Beroz, J.; Massuda, A.; Sloan, J.; Romeo, N.; Yu, Y.; Joannopoulos, J. D.; Kaminer, I.; Johnson, S. G.; Soljacic, M. A framework for scintillation in nanophotonics. *Science* **2022**, *375*, No. eabm9293.
(5) Bignell, L. J.; Mume, E.; Jackson, T. W.; Lee, G. P. Plasmonic light yield enhancement of a liquid scintillator. *Appl. Phys. Lett.* **2013**, *102*, 211902.
(6) Ye, W.; Yong, Z.; Go, M.; Kowal, D.; Maddalena, F.; Tjahjana, L.; Wang, H.; Arramel, A.; Dujardin, C.; Birowosuto, M. D.; Wong, L. J. The Nanoplasmonic Purcell Effect in Ultrafast and High-Light-Yield Perovskite Scintillators. *Adv. Mater.* **2024**, *36*, 2309410.
(7) Liu, B.; Zhu, Z.; Wu, Q.; Cheng, C.; Gu, M.; Xu, J.; Chen, H.; Liu, J.; Chen, L.; Ouyang, X. Plasmonic lattice resonance-enhanced light emission from plastic scintillators by periodical Ag nanoparticle arrays. *Appl. Phys. Lett.* **2017**, *110*, 181905.
(8) Long, O. Y.; Pajovic, S.; Roques-Carmes, C.; Tsurimaki, Y.; Rivera, N.; Soljačić, M.; Boriskina, S. V.; Fan, S. Nonreciprocal scintillation using one-dimensional magneto-optical photonic crystals. *arXiv* arXiv:2409.17002, 2024. DOI: 10.48550/arXiv.2409.17002.
(9) Zhang, J.; Liu, B.; Zhu, Z.; Wu, Q.; Cheng, C.; Liu, J.; Chen, L.; Ouyang, X.; Gu, M.; Xu, J.; et al. Enhanced light extraction of LYSO scintillator by photonic crystal structures from a modified porous anodized aluminum oxide layer. *Nuclear Instruments and Methods in Physics Research Section A: Accelerators, Spectrometers, Detectors and Associated Equipment* **2017**, *864*, 36−39.
(10) Singh, B.; Marshall, M. S.; Waterman, S.; Pina-Hernandez, C.; Koshelev, A.; Munechika, K.; Knapitsch, A.; Salomoni, M.; Pots, R.; Lecoq, P.; et al. Enhanced scintillation light extraction using nanoimprinted photonic crystals. *IEEE Trans. Nucl. Sci.* **2018**, *65*, 1059−1065.
(11) Martin-Monier, L.; Pajovic, S.; Abebe, M. G.; Chen, J.; Vaidya, S.; Min, S.; Choi, S.; Kooi, S. E.; Maes, B.; Hu, J.; Soljacic, M.; Roques-Carmes, C. Large-scale self-assembled nanophotonic scintillators for X-ray imaging. *Nat. Commun.* **2025**, *16*, 5750.
(12) Shultzman, A.; Segal, O.; Kurman, Y.; Roques-Carmes, C.; Kaminer, I. Enhanced imaging using inverse design of nanophotonic scintillators. *Advanced Optical Materials* **2023**, *11*, 2202318.
(13) Min, S.; Choi, S.; Pajovic, S.; Vaidya, S.; Rivera, N.; Fan, S.; Soljačić, M.; Roques-Carmes, C. End-to-end design of multicolor scintillators for enhanced energy resolution in X-ray imaging. *Light: Sci. Applications* **2025**, *14*, 158.
(14) Cassella, C. CT scans projected to result in 100,000 new cancers across the US. ScienceAlert, 2025; Accessed July 5, 2025, https://www.sciencealert.com/ct-scans-projected-to-result-in-100000-new-cancers-across-the-us.
(15) Smith-Bindman, R.; Chu, P. W.; Azman Firdaus, H.; Stewart, C.; Malekhedayat, M.; Alber, S.; Bolch, W. E.; Mahendra, M.; Berrington de Gonzalez, A.; Miglioretti, D. L. Projected lifetime cancer risks from current computed tomography imaging. *JAMA Internal Med.* **2025**, *185*, 710−719.
(16) Roques-Carmes, C.; Lin, Z.; Christiansen, R. E.; Salamin, Y.; Kooi, S. E.; Joannopoulos, J. D.; Johnson, S. G.; Soljacic, M. Toward 3D-printed inverse-designed metaoptics. *ACS Photonics* **2022**, *9*, 43−51.
(17) Yu, N.; Capasso, F. Flat optics with designer metasurfaces. *Nature materials* **2014**, *13*, 139−150.
(18) Chen, H.-T.; Taylor, A. J.; Yu, N. A review of metasurfaces: physics and applications. *Rep. Prog. Phys.* **2016**, *79*, No. 076401.
(19) Liu, Z.; Zhu, D.; Rodrigues, S. P.; Lee, K.-T.; Cai, W. Generative model for the inverse design of metasurfaces. *Nano Lett.* **2018**, *18*, 6570−6576.
(20) Li, Z.; Pestourie, R.; Lin, Z.; Johnson, S. G.; Capasso, F. Empowering metasurfaces with inverse design: principles and applications. *ACS Photonics* **2022**, *9*, 2178−2192.
(21) Melzer, J. E.; McLeod, E. 3D Nanophotonic device fabrication using discrete components. *Nanophotonics* **2020**, *9*, 1373−1390.
(22) Daqiqeh Rezaei, S.; Dong, Z.; You En Chan, J.; Trisno, J.; Ng, R. J. H.; Ruan, Q.; Qiu, C.-W.; Mortensen, N. A.; Yang, J. K. Nanophotonic structural colors. *ACS photonics* **2021**, *8*, 18−33.
(23) Michail, C.; Liaparinos, P.; Kalyvas, N.; Kandarakis, I.; Fountos, G.; Valais, I. Radiation detectors and sensors in medical imaging. *Sensors* **2024**, *24*, 6251.
(24) Li, Z.; Cheng, J.; Liu, F.; Wang, Q.; Wen, W.-W.; Huang, G.; Wu, Z. Research on the technological progress of CZT array detectors. *Sensors* **2024**, *24*, 725.
(25) Fredenberg, E.; Collin, D.; Carbonne, L.; Wu, M.; Man, B. D.; Grönberg, F. Simulating and correcting the pileup effect in deep-silicon photon-counting CT. *Med. Phys.* **2025**, *52*, No. e18075.
(26) Quirin, S.; Pavani, S. R. P.; Piestun, R. Optimal 3D single-molecule localization for superresolution microscopy with aberrations and engineered point spread functions. *Proc. Natl. Acad. Sci. U. S. A.* **2012**, *109*, 675−679.
(27) Shechtman, Y.; Sahl, S. J.; Backer, A. S.; Moerner, W. E. Optimal point spread function design for 3D imaging. *Phys. Rev. Lett.* **2014**, *113*, 133902.
(28) Booth, M. J. Adaptive optical microscopy: the ongoing quest for a perfect image. *Light: Science & Applications* **2014**, *3*, e165−e165.
(29) Dowski, E. R., Jr; Cathey, W. T. Extended depth of field through wave-front coding. *Applied optics* **1995**, *34*, 1859−1866.
(30) Goodman, J. W. *Introduction to Fourier Optics*, 3rd ed.; Roberts and Company Publishers: Greenwood Village, CO, 2005.
(31) Agostinelli, S.; Allison, J.; Amako, K. a.; Apostolakis, J.; Araujo, H.; Arce, P.; Asai, M.; Axen, D.; Banerjee, S.; Barrand, G.; et al. Geant4—a simulation toolkit. *Nuclear instruments and methods in physics research section A: Accelerators, Spectrometers, Detectors and Associated Equipment* **2003**, *506*, 250−303.
(32) *Ansys Zemax OpticStudio User Manual*, version 24.1; Ansys, Inc.: Canonsburg, PA, USA, 2025; Software documentation; available at https://optics.ansys.com/.
(33) Wiener, N. *Extrapolation, Interpolation, and Smoothing of Stationary Time Series: With Engineering Applications*; The MIT Press: Cambridge, MA, 1949. DOI: 10.7551/mitpress/2946.001.0001.
(34) Siewerdsen, J.; Antonuk, L.; El-Mohri, Y.; Yorkston, J.; Huang, W.; Cunningham, I. Signal, noise power spectrum, and detective quantum efficiency of indirect-detection flat-panel imagers for diagnostic radiology. *Medical physics* **1998**, *25*, 614−628.
(35) Maier, D. S.; Schock, J.; Pfeiffer, F. Dual-energy micro-CT with a dual-layer, dual-color, single-crystal scintillator. *Opt. Express* **2017**, *25*, 6924−6935.

https://doi.org/10.1021/acsphotonics.5c03124
ACS Photonics 2026, 13, 1757−1766

(36) Ran, P.; Yang, L.; Jiang, T.; Xu, X.; Hui, J.; Su, Y.; Kuang, C.; Liu, X.; Yang, Y. Multispectral Large-Panel X-ray Imaging Enabled by Stacked Metal Halide Scintillators. *Adv. Mater.* **2022**, *34*, 2205458.
(37) He, T.; Shao, W.; Yin, J.; Wang, H.; Zhou, Y.; Wang, J.-X.; Yuan, P.; Gutiérrez-Arzaluz, L.; Wu, W.; Zhou, R.; et al. Multi-energy X-ray imaging enabled by ΔE-E telescope scintillator. *Matter* **2024**, *7*, 2521−2535.
(38) Maurino, S. L.; Badano, A.; Cunningham, I. A.; Karim, K. S. Theoretical and Monte Carlo optimization of a stacked three-layer flat-panel x-ray imager for applications in multi-spectral medical imaging. In *Medical Imaging 2016: Physics of Medical Imaging*; Proceedings of SPIE; SPIE: 2016; p 97833Z. DOI: 10.1117/12.2217085.
(39) Alvarez, R. E.; Macovski, A. Energy-selective reconstructions in x-ray computerised tomography. *Physics in Medicine & Biology* **1976**, *21*, 733.
(40) Molesky, S.; Lin, Z.; Piggott, A. Y.; Jin, W.; Vucković, J.; Rodriguez, A. W. Inverse design in nanophotonics. *Nat. Photonics* **2018**, *12*, 659−670.
(41) Johnson, S. G.; Schueller, J. Nlopt: Nonlinear optimization library. *Astrophysics Source Code Library*, 2021, ascl-2111.004.
(42) Sitzmann, V.; Diamond, S.; Peng, Y.; Dun, X.; Boyd, S.; Heidrich, W.; Heide, F.; Wetzstein, G. End-to-end optimization of optics and image processing for achromatic extended depth of field and super-resolution imaging. *ACM Transactions on Graphics (TOG)* **2018**, *37*, 1−13.
(43) Zernike, v. F. Beugungstheorie des schneidenver-fahrens und seiner verbesserten form, der phasenkontrastmethode. *Physica* **1934**, *1*, 689−704.
(44) Shepp, L. A.; Logan, B. F. The Fourier reconstruction of a head section. *IEEE Transactions on nuclear science* **1974**, *21*, 21−43.
(45) Jürgensen, M.; Vaidya, S.; Pajovic, S.; Gales, J. P.; Chen, J.; Katznelson, S.; Kooi, S. E.; Richards, S.; Braddock, I.; Armstrong, C. D.; Kaminer, I.; Soljačić, M.; Rechtsman, M. C.; Roques-Carmes, C. Volumetrically-Patterned Nanophotonic Scintillators. In *Proceedings of CLEO 2025: Technical Digest Series*; Optical Publishing Group: Long Beach, CA, 2025; paper SS184_7.
(46) Chou, S. Y.; Krauss, P. R.; Renstrom, P. J. Nanoimprint lithography. *Journal of Vacuum Science & Technology B: Microelectronics and Nanometer Structures Processing, Measurement, and Phenomena* **1996**, *14*, 4129−4133.
(47) Zhang, J.; Li, Y.; Zhang, X.; Yang, B. Colloidal self-assembly meets nanofabrication: From two-dimensional colloidal crystals to nanostructure arrays. *Advanced materials* **2010**, *22*, 4249−4269.
(48) Mai, Y.; Eisenberg, A. Self-assembly of block copolymers. *Chem. Soc. Rev.* **2012**, *41*, 5969−5985.
(49) Wu, E.-S.; Strickler, J. H.; Harrell, W. R.; Webb, W. W. Two-photon lithography for microelectronic application. *Proc. SPIE 1674, Optical/Laser Microlithography V* **1992**, 776−782.
(50) Chen, J.; Pajovic, S.; Vaidya, S.; Michaels, W.; Pontula, S.; Choi, S.; Martin-Monier, L.; Roques-Carmes, C.; Soljačić, M. Phase mask metasurfaces for high-resolution X-ray imaging. In *Proceedings of CLEO: Applications & Technology 2025*; Optical Publishing Group: Long Beach, CA, 2025; paper AA137_2.
(51) Lin, Z.; Pestourie, R.; Roques-Carmes, C.; Li, Z.; Capasso, F.; Soljačić, M.; Johnson, S. G. End-to-end metasurface inverse design for single-shot multi-channel imaging. *Opt. Express* **2022**, *30*, 28358−28370.
(52) Roques-Carmes, C.; Wang, K.; Yang, Y.; Majumdar, A.; Lin, Z. Metaoptic Computational Imaging. *ACS Photonics* **2025**, *12*, 1722−1733.

https://doi.org/10.1021/acsphotonics.5c03124
ACS Photonics 2026, 13, 1757−1766